ROYAL SOCIETY OF CHEMISTRY

EDGE ARTICLE

Single-crystal-ordered-mesoporous metal nitrides without intrinsic Raman signals for highly sensitive SERS detection

Linchangqing Yang,[a] Yijing Zong,[a] Meng Yin,[a] Wencai Yi, [ID] [d] Junfang Li,[a] Jie Lin, [ID] *[c] Qinghong Kong [ID] *[b] and Guangcheng Xi [ID] *[a]

The formation of transition metal nitrides (TMNs) necessitates overcoming extremely high reaction barriers, which renders the precise synthesis of TMN materials with tailored structures a significant challenge. Herein, we propose a molten-salt/template strategy for the accurate customization of TMNs featuring a rare single-crystal ordered mesoporous (SCOM) structure. By leveraging this strategy, 5 types of SCOM-structured TMNs—including WN, MoN, TiN, VN, and CoN were synthesized. Hydroxylation of templates and the subsequent formation of SCOM-structured metal oxides were identified as the key factors governing the formation of SCOM-TMNs. Interestingly, these SCOM-structured WN lack the intrinsic Raman signals typically possessed by non-metallic materials, effectively resolving the long-standing issue of background interference in non-metallic surface-enhanced Raman scattering (SERS) substrates. The WN substrate achieves an ultrahigh Raman enhancement factor of up to 7.5×10^7 and an ultralow detection limit of 1×10^{-12} M.

Introduction

Transition metal nitrides (TMNs) constitute a significant category of interstitial compounds. Within these compounds, nitrogen atoms are arranged in an orderly manner at the interstitial sites of the transition metal lattice. The formation of metal–nitrogen (M–N) bonds triggers two notable phenomena: the expansion of the metal lattice and the contraction of the metal d-band. Together, these effects contribute to an elevation in the density of states (DOS).[1,2] These structural and electronic alterations endow TMNs with intriguing and valuable metal-like characteristics. Specifically, they exhibit high electrical conductivity, a robust localized surface plasmon resonance (SPR) effect, and catalytic performance analogous to that of platinum. Owing to these properties, TMNs have found widespread applications in domains such as microelectronics, chemical sensing, and energy conversion.[3–9] Furthermore, in comparison to platinum-group metals, TMNs possess a distinct advantage: the introduction of nitrogen defects enables the

more straightforward creation of abundant active sites. This not only facilitates the occurrence of interfacial reactions but also enhances reaction efficiency.[10–12] Of particular significance, metal-like TMNs, including WN, MoN, VN, and TiN, demonstrate exceptional conductivity, thermal stability, and corrosion resistance. These attributes render them suitable for applications under extremely harsh conditions, such as high temperatures, irradiation, and strong acid or alkali environments, thereby broadening their scope of application.[13–20] Additionally, unlike platinum-group metals, TMNs are more abundantly available in nature, leading to a considerably lower utilization cost.

High specific surface area and high porosity are effective approaches to enhancing material properties. In recent years, functional TMN materials with high specific surface area have garnered significant attention, and their synthesis methods have been continuously refined.[21–23] In early synthesis strategies, the target TMNs were synthesized by directly heating the corresponding metal precursors with nitrogen gas.[24,25] However, due to the unfavorable thermodynamics of the nitridation reaction, this method typically requires high temperatures (>1000 °C) and pressures (several GPa) to overcome the extremely high reaction barrier. These harsh conditions often result in severe grain sintering and a small specific surface area of the final product (<10 m^2 g^{-1}). Subsequent studies revealed that replacing nitrogen with ammonia, a more chemically reactive gas effectively reduces the required synthesis temperature and pressure, thereby increasing the specific surface area of the resulting TMNs. As a result, ammonia-assisted thermal

[a] *Key Laboratory of Consumer Product Quality Safety Inspection and Risk Assessment for State Market Regulation, Chinese Academy of Quality and Inspection & Testing, Beijing 100176, China. E-mail: xiguangcheng@caiq.org.cn*

[b] *School of the Environment and Safety Engineering, Jiangsu University, Zhenjiang 212013, China. E-mail: kongqh@ujs.edu.cn*

[c] *Laboratory of Advanced Theranostic Materials and Technology, Ningbo Institute of Materials Technology and Engineering, Chinese Academy of Sciences, Ningbo 315201, China. E-mail: linjie@nimte.ac.cn*

[d] *School of Physics and Physical Engineering, Qufu Normal University, Qufu 273165, China*

nitridation has become the dominant method for TMN synthesis at present.[26–31] Recently, with the emergence of molten-salt-assisted synthesis as a cutting-edge technique, the unique properties of molten salts enable them to play distinct roles in the synthesis process. This advancement has made it feasible to synthesize TMN materials with a high specific surface area and special structures, such as layered, sheet-like, and spongy morphologies.[9,32–34]

Surface-enhanced Raman spectroscopy (SERS), renowned for its ultra-high sensitivity and fingerprint identification capability, has become a pivotal tool in fields such as analytical chemistry, biosensing, and environmental monitoring.[35–38] In recent years, a class of TMNs exhibiting quasi-metallic properties has attracted widespread attention. These materials possess excellent chemical stability, tunable optical properties, and localized surface plasmon resonance (LSPR) behavior similar to noble metals, positioning them as highly promising alternatives to precious metals.[39,40] However, most current SERS studies based on TMNs still focus on solid thin films, disordered nanoparticles, or simple two-dimensional nanostructures.[41–43] When applied to more practically relevant solution-phase detection, these structures face a fundamental bottleneck: target molecules struggle to efficiently reach the limited surface hot-spot regions via passive diffusion. As a result, the intrinsic electromagnetic enhancement capability of the materials is not fully utilized, limiting overall sensitivity and reliability.

Over the past decade, while researchers have developed various methods to synthesize TMN materials with distinct morphologies, there remains a lack of effective synthetic strategies to precisely control the structure and composition of TMNs.[44–47] For instance, the conventional ammonia thermal method requires the insertion of nitrogen atoms into the metal lattice or the substitution of oxygen atoms in the corresponding metal oxide at elevated temperatures conditions that easily lead to sample fragmentation. The molten-salt method can effectively mitigate such issues,[48,49] nevertheless, the molten-salt method also introduces uncertainty regarding the product structure, and it is often challenging to predict the morphology of the resulting nitrided products. Although TMNs have been widely applied across numerous fields, there is still a shortage of customized morphological structures featuring high specific surface areas and high porosity—attributes that are critical to unlocking their full performance potential. Thus, developing precise synthesis methods for TMN materials with high crystallinity, high specific surface area, high porosity, and tailored compositions and structures holds great significance.

Herein, we propose a molten-salt/template strategy for precise synthesis of TMN materials with customized structures. These products exhibit rare SCOM characteristics in their structure. Based on this molten-salt/template strategy, 5 kinds of SCOM-TMNs were synthesized. Hydroxylation and the consequent formation of SCOM-structured metal oxides were identified as the key factors governing the formation of the SCOM-TMNs. As an important application, these SCOM WNs synthesized by us exhibit extraordinary SERS sensing properties, with Raman EF up to 7.5×10^7, and the lowest detection limit is as low as 1×10^{-12} M. The current research results provide a feasible method for the precise synthesis of TMN materials with adjustable structure and composition.

Results and discussion

Synthesis and characterization of SCOM-WN

As illustrated in Fig. 1a, TMNs with SCOM structure were synthesized via a proposed molten-salt/template strategy. To elaborate on this strategy, the preparation process of SCOM-WN sample is taken as an example, and the detailed steps are as follows: commercially available ordered mesoporous SBA-15 (serving as the template; its morphology is presented in Fig. S1) was immersed in H_2O_2 solution and subjected to ultrasonication for 10 min, which treatment was intended to achieve hydroxylation of SBA-15. The hydroxylated SBA-15 was then impregnated in an anhydrous ethanol solution of tungsten hexachloride (WCl_6). Leveraging the bonding interaction of hydroxyl groups and the capillary effect of mesoporous channels, W^{6+} ions were effectively adsorbed and anchored inside the channels of SBA-15. Once SBA-15 had sufficiently adsorbed W^{6+} ions, the W^{6+}/SBA-15 composite was separated from the ethanol solution by centrifugation. Subsequently, it was vacuum freeze-dried at -80 °C. The dried W^{6+}/SBA-15 product was thoroughly mixed with KCl (used as the molten salt). The mixture was placed in a tube furnace, and a mixture of NH_3 and N_2 was introduced into the furnace. The temperature was slowly raised to 600 °C to carry out the nitridation reaction. After the completion of nitridation, deionized water was used to remove the KCl molten salt, and NaOH was employed to eliminate the SBA-15 template.

The morphology and structure of the as-prepared WN samples were characterized systematically. As presented in Fig. 1b, X-ray powder diffraction (XRD) pattern of the product exhibits characteristic peaks at 37.3°, 43.6°, 63.3°, and 75.7°, which can be indexed to the (111), (200), (220), and (311) crystal planes of cubic-phase WN (JCPDS no. 75-1012), respectively. Fig. 1c displays the scanning electron microscope (SEM) image of the sample, revealing a highly regular and ordered mesoporous structure with ortho-hexagonal pore walls. This well-defined structure is attributed to the template effect of SBA-15. The transmission electron microscope (TEM) images of the sample are shown in Fig. 1d and e; both the dark-field image (Fig. 1d) and bright-field image (Fig. 1e) clearly visualize this highly ordered mesoporous architecture, with a pore size of approximately 5–7 nm and a pore wall thickness of around 3–5 nm. Fig. 1f present the high-resolution TEM (HRTEM) image of the sample, indicating that the WN material possesses high crystallinity. Notably, the HRTEM images reveal that these ordered mesoporous structures not only exhibit high crystallinity but also feature highly uniform lattice stripe orientations throughout the entire structure. This unique combination forms a very rare type of SCOM structure. Large-scale HRTEM images provide more distinct evidence for this structural feature (Fig. S2). Furthermore, the selected area electron diffraction (SAED) pattern of this region (Fig. S3) shows a typical single-crystal cubic-phase diffraction pattern, which further verifies the SCOM characteristics. Additionally, the mutually
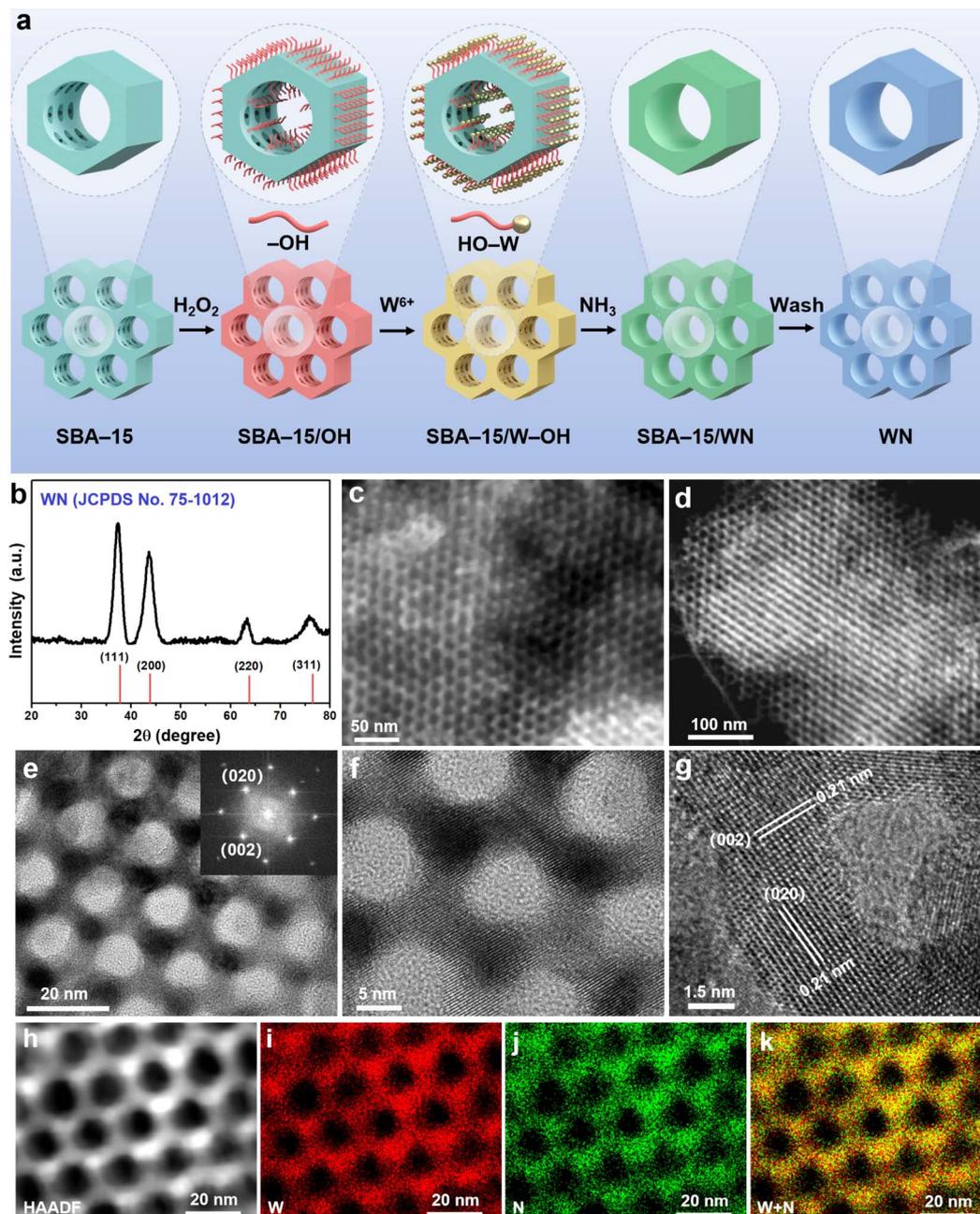
Fig. 1 Synthesis and characterization of the SCOM-WN synthesized with SBA-15 as template. (a) Schematic illustrating the molten-salt/template strategy. (b) XRD pattern. (c) SEM image. (d) HAADF image. (e) TEM image, inset: FFT pattern. (f and g) HRTEM images. (h) HAADF image. (i–k) EDS mapping images.

perpendicular crystal planes with a lattice spacing of 0.21 nm can be indexed to the (002) and (020) crystal planes of cubic-phase WN, as illustrated in Fig. 1g.

Energy-dispersive X-ray spectroscopy (EDS) mapping images (Fig. 1h–k) illustrate the uniform distribution of W and N elements throughout the mesoporous structure. Furthermore, the atomic ratio of W to N is determined to be 1.05 : 1, which is in excellent agreement with the stoichiometric ratio of WN (Fig. S4). To gain deeper insights into the product's composition and chemical state, X-ray photoelectron spectroscopy (XPS) analysis was performed. In the XPS survey spectrum, the high-resolution spectra of W 4f and N 1s confirm the formation of cubic-phase WN from the perspective of valence states. These spectra also verify the high purity of the WN product; the weak W^{6+} signal observed can be ascribed to the slight oxidation of the WN surface, which leads to the formation of trace amounts of WO_3 (Fig. S5). In comparison with previously reported TMN materials, the SCOM-WN products exhibit higher specific surface area and pore volume (Table S1). Nitrogen adsorption–desorption measurements reveal that the SCOM-WN samples have a specific surface area of 135.6 $m^2 g^{-1}$ and a pore volume of 0.45 $cm^3 g^{-1}$, respectively. Additionally, the pore size

distribution presents a distinct peak at 6.3 nm (Fig. S6), which is consistent with the observations from TEM images.

Formation mechanism of SCOM-WN

The hydroxylation treatment of SBA-15 plays a crucial role in the formation of SCOM structures. This conclusion is primarily supported by the following experimental observations. When the temperature of the tube furnace is increased to 150 °C, 200 °C, and 300 °C, the collected intermediate products were identified as amorphous and crystalline WO_3 (Fig. 2a–c and S7); notably, the WO_3 obtained at 300 °C exhibits distinct SCOM structures. Based on these key observation, it can be inferred that during the heating process, the tungsten ions adsorbed within the pores of SBA-15 undergo hydrolysis with hydroxyl groups to form WO_3. Subsequent observations indicate that these SCOM-structured WO_3 intermediate products were first converted into amorphous WN during the nitridation process (Fig. 2d, S8a and b). With the extension of reaction time, these amorphous WN gradually transformed into crystalline WN while maintaining the characteristics of the SCOM structure (Fig. 2e, f and S8c–f).

These observational results revealed that it is precisely the initial formation of SCOM-structured WO_3 that enables the subsequent generation of SCOM-structured WN. Thus, hydroxylation serves as an indispensable prerequisite for the formation of SCOM-TMNs. To further substantiate this conclusion, a set of comparative experiments was conducted. The results revealed that when non-hydroxylated SBA-15 was used as the template and all other experimental procedures kept consistent, no WO_3 intermediates were detected during the heating process (from room temperature to 300 °C). Instead, the nitrided product was found to be random particle aggregates of WN
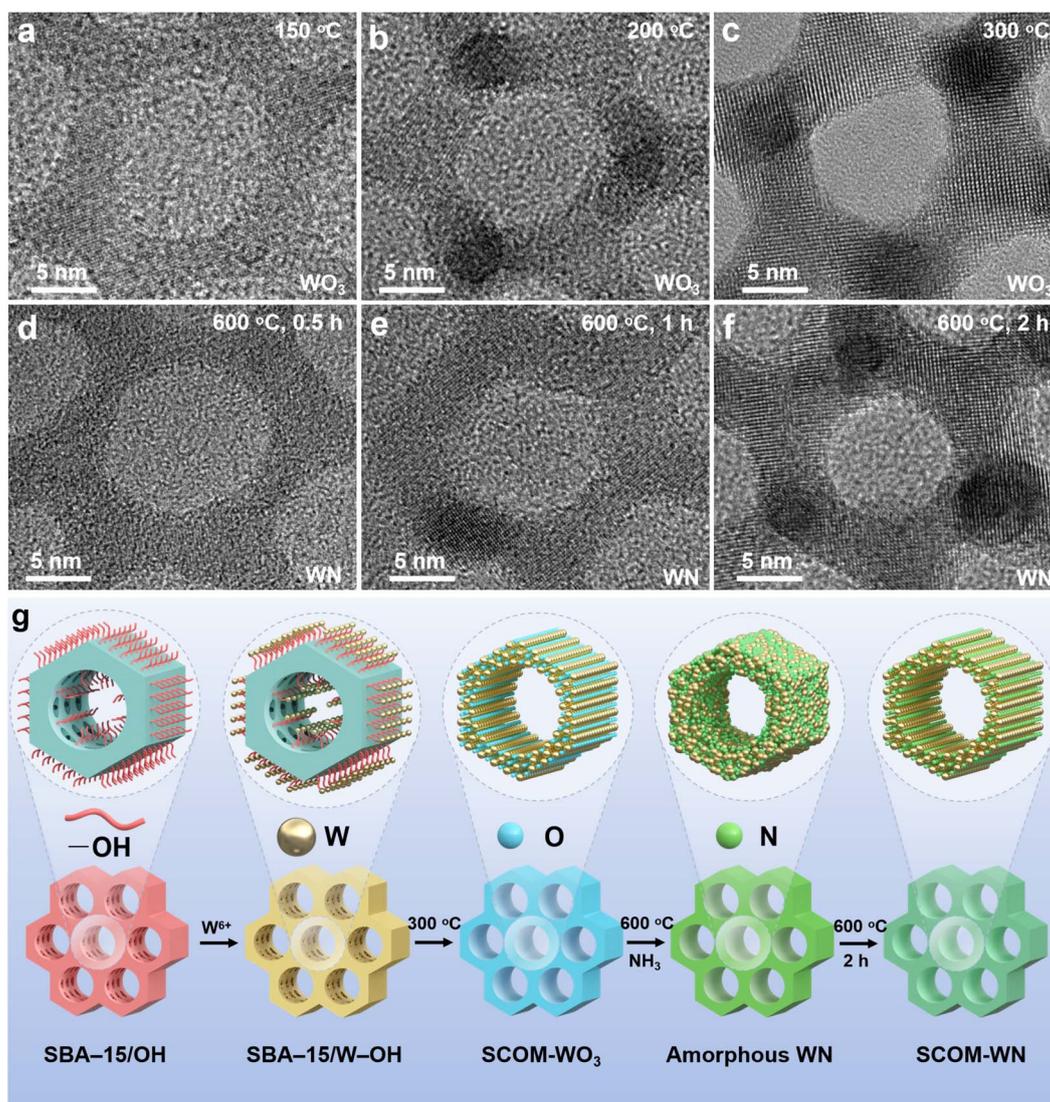

Fig. 2 Formation mechanism of the SCOM-WN. (a) Amorphous WO_3 obtained at 150 °C. (b) Partially crystallized WO_3 obtained at 200 °C. (c) Crystalline WO_3 obtained at 300 °C. (d) Amorphous WN obtained after 0.5 h of nitriding. (e) Partially crystallized WN obtained after 1 h of nitriding. (f) Crystalline WN obtained after 2 h of nitriding. (g) Schematic diagram of the proposed hydroxylation-induced molten salt/template synthesis mechanism.

(Fig. S9). Collectively, these results confirm the critical role of hydroxylation in the formation of SCOM structures. Moreover, for the first time in the experiment, the transition from amorphous to single crystal during the nitridation process of metal oxides with SCOM structure in confined space was observed, providing a new perspective for understanding the formation of SCOM-TMN structures. Fig. 2g illustrates the proposed mechanism underlying hydroxylation-induced SCOM structure formation.

Furthermore, with all other experimental conditions held constant, in the absence of the SBA-15, WCl_6 directly reacted with NH_3 in molten KCl. The obtained product consisted of crystalline WN nanosheets with a thickness of approximately 5–7 nm (Fig. S10). This result demonstrates that SBA-15 exerts an indispensable templating effect on the formation of SCOM-WN.

The influence of molten salt on the experimental outcomes was also examined. When the W^{6+}/SBA-15 composite was directly exposed to NH_3 for nitridation treatment, the final product was irregular particle aggregates (Fig. S11). This finding indicates that molten KCl functions to isolate WN grains during the nitridation process, thereby preventing sintering. Collectively, these comparative experimental results unequivocally confirm that both the SBA-15 template and molten KCl are indispensable to the successful preparation of such SCOM-structured TMN materials.

Synthesis and characterization of SCOM-TMNs (MoN, VN, TiN, CoN)

Employing this molten-salt/template strategy, we successfully prepared not only SCOM-structured WN but also MoN, VN, TiN,
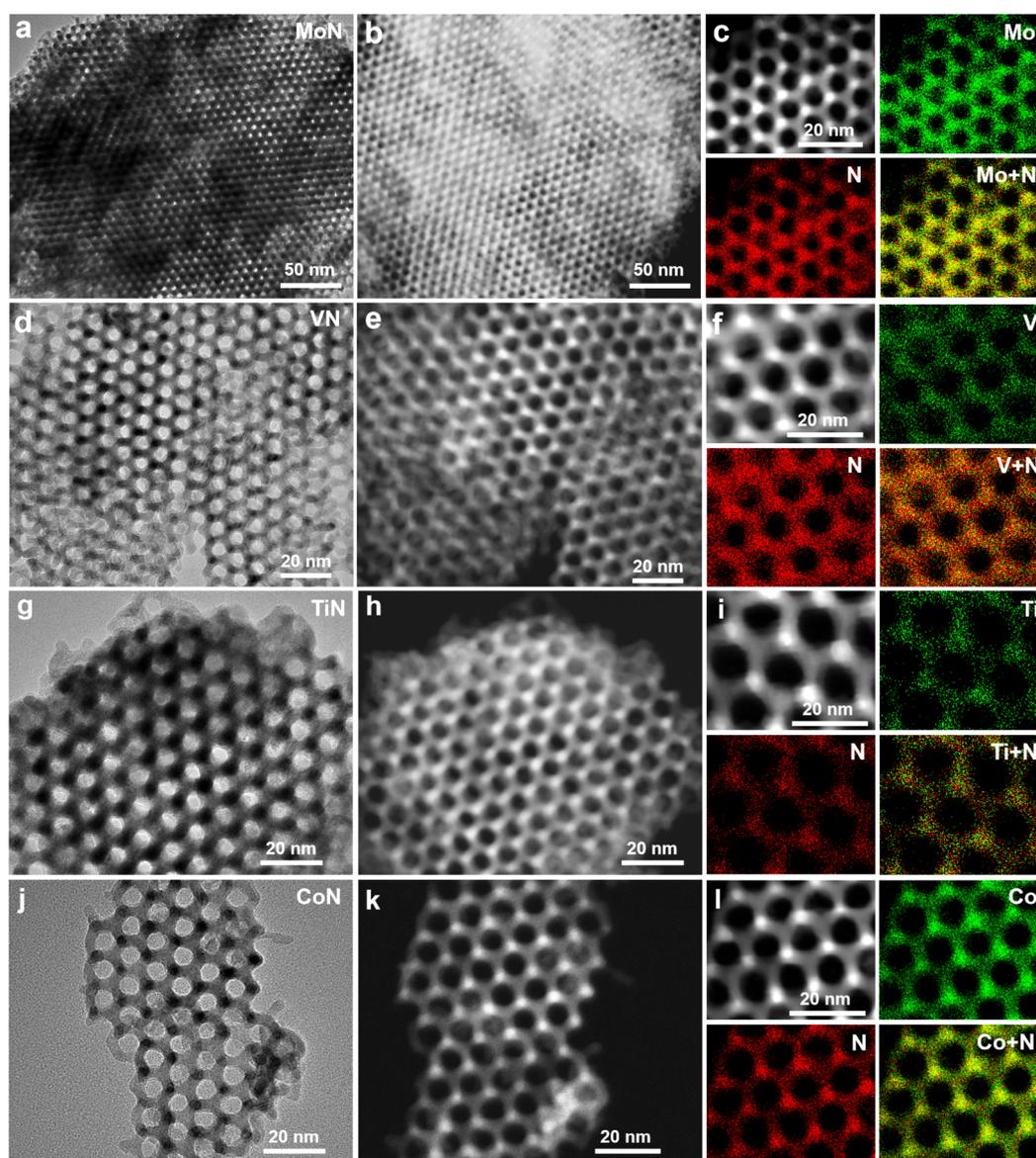

Fig. 3 Structure and composition of the SCOM-TMNs (MoN, WN, TiN, CoN) synthesized with SBA-15 as template. (a–c) TEM, HAADF and EDS mapping images of the SCOM-MoN. (d–f) TEM, HAADF and EDS mapping images of the SCOM-VN. (g–i) TEM, HAADF and EDS mapping images of the SCOM-TiN. (j–l) TEM, HAADF and EDS mapping images of the SCOM-CoN.

and CoN with analogous morphology and structure. TEM images (Fig. 3a, d, g, and j) and HAADF images (Fig. 3b, e, h, and k) reveal that these four samples possess a highly similar framework structure to the aforementioned SCOM-WN. Furthermore, large-area HRTEM images demonstrate that these four samples also exhibit high crystallinity and display large-area SCOM characteristics (Fig. S12–S15). EDS mapping images of MoN, VN, TiN, and CoN confirm the uniform distribution of nitrogen and the corresponding metal elements within each sample (Fig. 3c, f, i, and l).

The specific surface areas of MoN, VN, and TiN were determined to be 113.5 m^2 g^{-1}, 124.7 m^2 g^{-1}, 117.9 m^2 g^{-1}, and 103.8 m^2 g^{-1}, respectively (Fig. S16). Additionally, XRD patterns, EDS spectra, and XPS spectra comprehensively verified the successful synthesis of MoN, VN, TiN, and CoN from the perspectives of crystal phase, elemental composition, and oxidation state of constituent elements, respectively (Fig. S17–S19). These outcomes underscores the versatility of the molten-salt/template strategy for fabricating SCOM-structured TMNs with high specific surface area.

SERS properties of SCOM-WN

Density functional theory (DFT) calculations reveal that the energy levels of cubic-phase WN near the Fermi level are composed of W 5d orbitals, endowing the material with distinct metallic-like properties (Fig. 4a). Furthermore, the free electron
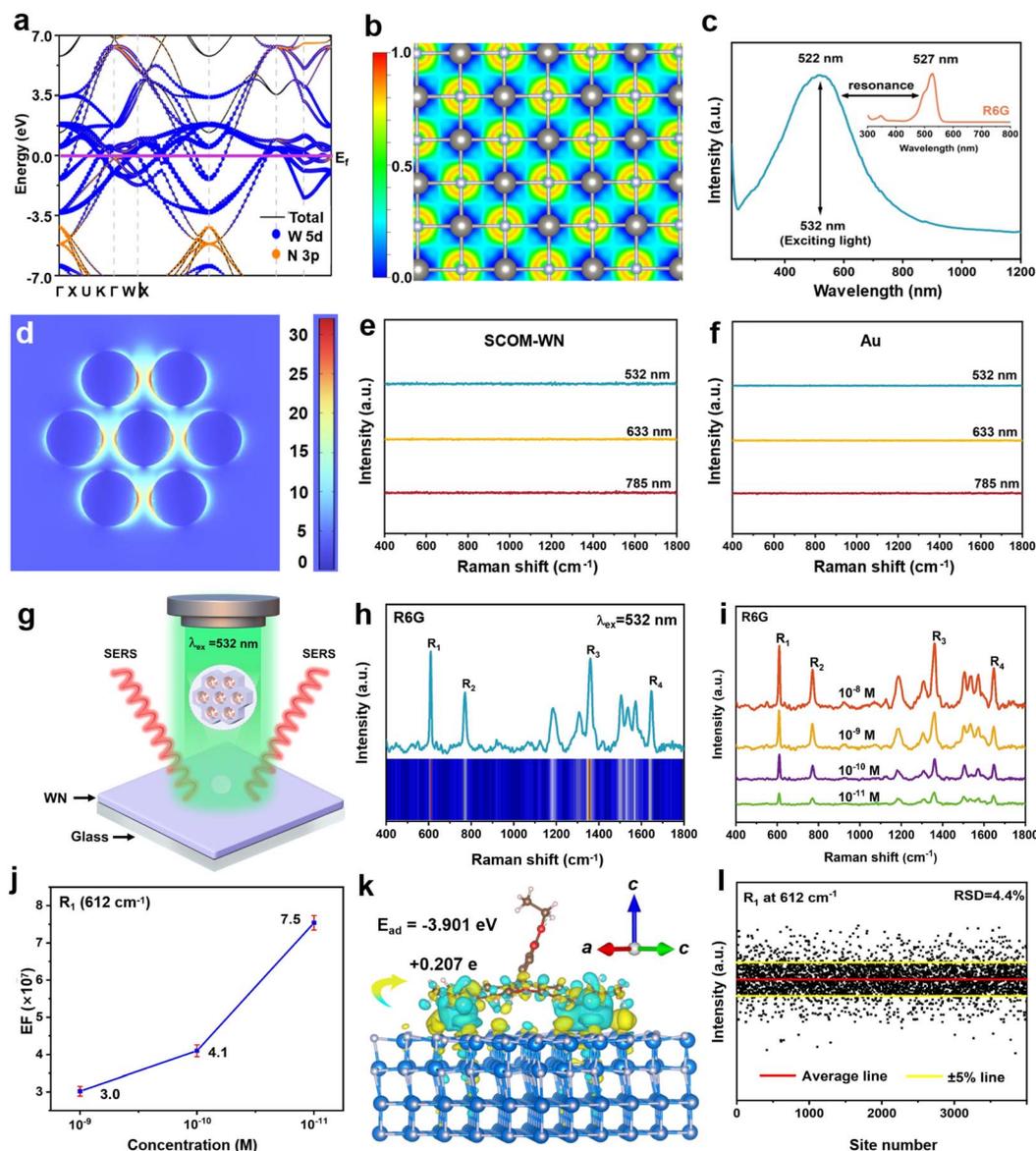

Fig. 4 SERS properties of the SCOM-WN. (a) Electronic density of states of cubic WN. (b) ELF of cubic WN. (c) LSPR effect. (d) Simulated hot-spot distribution of the SCOM-WN. (e) Raman spectra of the SCOM-WN. (f) Preparation of SERS substrates via spin-coating method. (g) Schematic diagram for SERS Experiments. (h) Raman spectrum of 1 × 10^{-7} M R6G. (i) Raman spectrum of R6G with different concentrations. (j) The average Raman EFs obtained by counting the peak intensities (R_1) at three different concentrations. (k) Side views of the electron density difference isosurfaces for R6G chemisorbed onto the surface of SCOM-WN. (l) RSD of R_1 of 1 × 10^{-9} M R6G.

gas (FEG) distribution map, derived from electron localization function (ELF) simulations, demonstrates a high FEG density for cubic-phase WN (Fig. 4b). Owing to these prominent metallic characteristics, UV-visible absorption spectroscopy shows that the SCOM-WN exhibits a strong localized surface plasmon resonance (LSPR) effect in the visible light region, with an absorption peak centered at 522 nm (Fig. 4c). This phenomenon can be attributed to the high density free electrons respond to incident light. It should be noted that this LSPR wavelength is close to the 532 nm excitation light commonly used in Raman tests, and is also close to the absorption wavelength (527 nm) of the most frequently used probe molecule, Rhodamine 6G (R6G), facilitating electromagnetic field resonance enhancement. Leveraging this robust localized-SPR effect, finite-difference time-domain (FDTD) simulations were performed on the SCOM-WN. The simulation results indicate that under excitation light with a wavelength of 532 nm, the SCOM-WN samples generate a strong near-field effect, leading to the formation of numerous electromagnetic field hotspots (Fig. 4d). The maximum electromagnetic field enhancement factor (EF) is 32.6, corresponding to a Raman EF of up to 1.13×10^6.

These experimental and computational findings confirm that SCOM-WN samples hold great promise as metallic-like SERS substrates. More notably, unlike semiconductor-based SERS substrates, the SCOM-structured WN itself exhibits no intrinsic Raman scattering peaks. As illustrated in Fig. 4e, no signal features were detected in the Raman spectra of these SCOM-WN samples when excited by three of the most commonly used wavelengths (532 nm, 633 nm, and 785 nm). These results suggest that the plasmonic oscillations generated by the free electrons in WN induce a strong shielding effect in the visible light range, preventing photons from effectively coupling with lattice vibrations, and thus precluding the formation of observable Raman signals.

To validate this conclusion, we conducted identical tests using prepared Au nanoparticles; the results were nearly consistent with those of SCOM-WN (Fig. S20a). For comparison, we also repeated the aforementioned tests using previously reported semiconductor-based SERS substrate materials. The results showed that typical semiconductor SERS substrate materials, including TiO_2, $W_{18}O_{49}$, and MoO_2,[50–52] all exhibited intense intrinsic Raman spectra without exception (Fig. S20b–d). The intrinsic Raman spectrum of a substrate inevitably causes severe interference with the SERS signal of the analyte. Therefore, the unique characteristic of SCOM-WN, acting as a non-metallic SERS substrate with no intrinsic Raman scattering, undoubtedly constitutes a significant advantage for its practical SERS applications.

To thoroughly investigate the surface-enhanced Raman scattering (SERS) properties of the as-prepared SCOM-WN, we utilized it as a Raman substrate. The SERS substrates were fabricated by spin-coating the SCOM-WN powders onto glass slides (Fig. 4f and S21). R6G was selected as the probe molecule, and the laser excitation conditions were set as follows: an excitation wavelength of 532 nm, a laser power of 0.7 mW, and a laser beam incident perpendicularly to the substrate plane

(Fig. 4g). EDS mapping images show that these R6G molecules can penetrate deep into the channels, indicating that the SCOM-WN substrate has excellent adsorption capacity for R6G molecules (Fig. S22). On this SCOM-WN substrate, the Raman signals of R6G molecules at a concentration of 1×10^{-7} M were clearly distinguishable (Fig. 4h). Detection results for a series of R6G samples with varying concentrations revealed that the WN substrate exerted a significant Raman enhancement effect on R6G within the concentration range of 1×10^{-8}–1×10^{-11} M (Fig. 4i). It is worth noting that due to the absence of Raman spectroscopy in WN itself, background interference is eliminated. Therefore, even if the concentration of R6G is as low as 1×10^{-12} M, distinguishable R6G signals is still obtained on the substrate (Fig. S23). To the best of our knowledge, such high sensitivity ranks among the top performers for non-metallic SERS substrates (Table S2). Furthermore, a good linear relationship between R6G concentration and Raman signal intensity was observed in the concentration range of 1×10^{-7}–1×10^{-11} M (Fig. S24), which lays a foundation for quantitative analysis.

By calculating the Raman EF based on the scattering peak intensity of R_1 at 612 cm^{-1}, the EF of the SCOM-WN substrate for R6G molecules was determined to be 7.5×10^7 (Fig. 4j, see the SI for detailed calculation procedures). This strong Raman EF is fully comparable to that of noble-metal SERS substrates (Table S3). It is interesting that the measured EF (7.5×10^7) is one order of magnitude higher than the EF (1.13×10^6) calculated solely by electromagnetic field enhancement theory, indicating that there are other enhancing factors at play. Theoretical calculations indicate that there is a significant chemical adsorption between the WN substrate and R6G molecules, with an adsorption energy of approximately 3.901 eV (Fig. 4k). Furthermore, formula calculations show that there is a significant interface charge transfer effect between R6G molecules and SCOM-WN, with a charge transfer amount of 0.207 e. These results indicate that chemical enhancement caused by interface charge transfer (ICT) also exists in the WN-R6G system.[52–54] Therefore, the high Raman EF can be ascribed to the synergistic enhancement mechanism, which arises from the strong localized-SPR effect and ICT effect of these SCOM-WN substrates.

The SCOM-WN substrate also demonstrates excellent signal uniformity. Taking R6G (1×10^{-9}) as an example, its Raman mapping image reveals an extremely uniform signal distribution (Fig. S25). For a more objective assessment of signal uniformity, the peak intensities of R_1 at 4000 discrete points across 2 cm^2 area of the substrate were counted. Calculations showed that the relative standard deviation (RSD) of the R_1 signal intensity was merely 4.4% (Fig. 4l), indicating superior uniformity compared to noble metal array-based SERS substrates.[55,56] Such a low RSD value, coupled with a good concentration-signal linear relationship, can be attributed to the uniform SCOM structure, an obvious advantage when SERS is applied to quantitative detection.

The versatility and stability of the WN substrate were evaluated systematically. A series of high-risk chemicals were selected as probe molecules to investigate their Raman signals on the substrate. The results indicated that the substrate

exhibited an extremely sensitive response to crystal violet (CV), melamine (MA), bisphenol A (BPA), 2,4-dichlorophenol (2,4-DCP), 2,4,5-trichlorophenol (2,4,5-TCP), and 2,3,5,6-tetrachlorophenol (2,3,5,6-TECP) across a concentration range of 1×10^{-7} to 1×10^{-11} M (Fig. 5a–f). In the corrosion resistance test, the substrate was immersed in 5 M HCl or 5 M NaOH solutions for 3 h. Experimental results revealed that the substrate retained its intact morphology and crystal lattice (Fig. 5g, h, S26 and S27), with an almost unchanged crystalline phase (Fig. S28 and S29). We have performed ten repeated measurements on the same substrate and found that the Raman spectra showed almost no variation. (Fig. S30). Additionally, the sample exhibited remarkable thermal stability and

oxidation resistance: it remained stable even when heated to 300 °C in air for 1 h (Fig. 5i and S31), and the SERS performance of the samples stored in air for three months remains almost unchanged (Fig. S32). Thermogravimetric analysis (TGA) further showed that the sample was completely oxidized to WO$_3$ only when the temperature reached 524 °C (Fig. S33). These findings strongly confirm that the WN substrate possesses excellent corrosion resistance and thermal stability, laying a solid foundation for its practical applications. In addition, other substrates based on SCOM-structured TMNs have also exhibited excellent SERS activity (Fig. 5j–l), which further demonstrates that SCOM-structured TMNs represent a highly promising class of non-metallic SERS substrates.
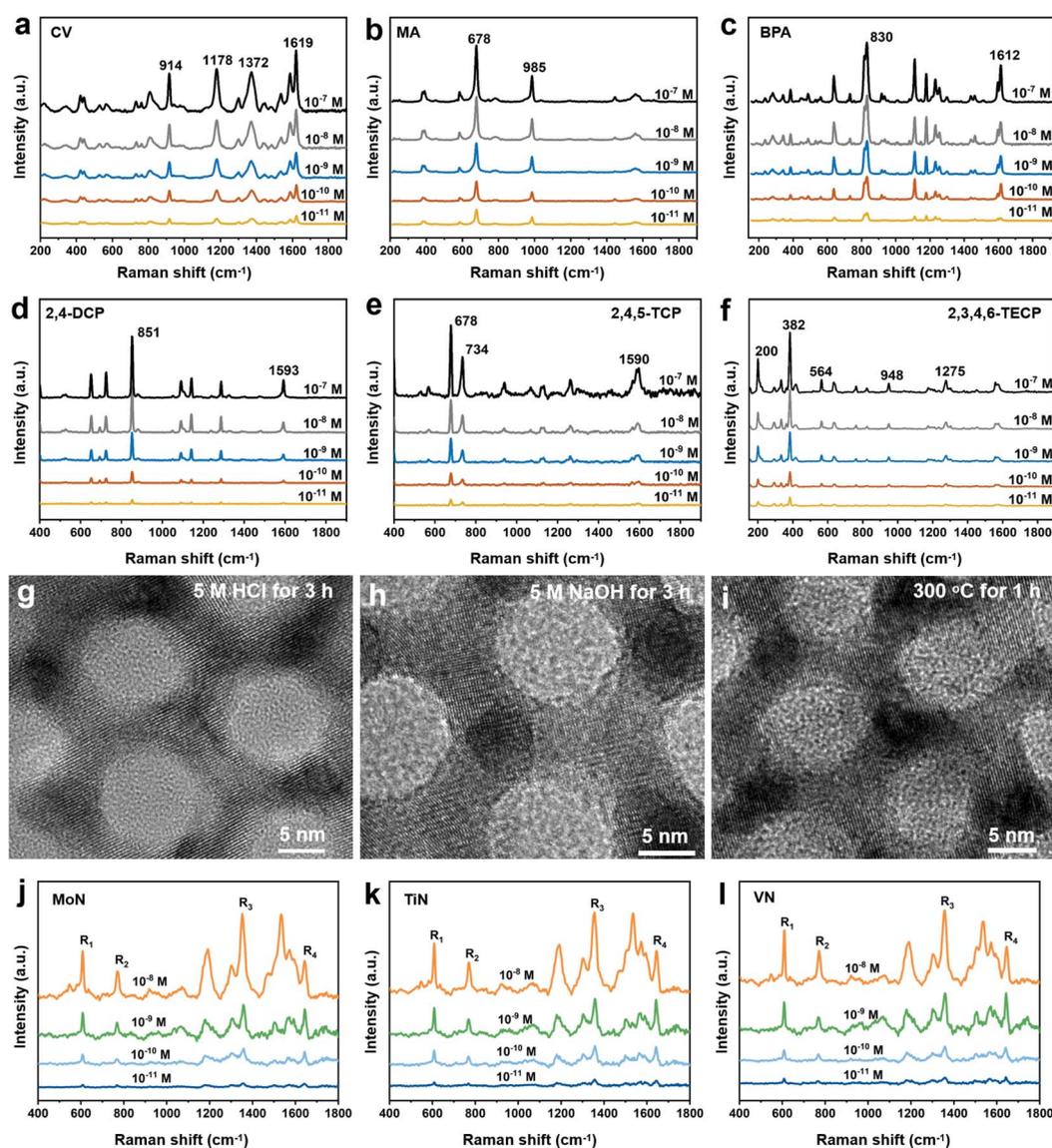

Fig. 5 Versatility and stability of the SCOM-TMN substrates. (a–f) Raman spectra of a series of environmental pollutants: (a) CV, (b) MA, (c) BPA, (d) 2,4-DCP, (e) 2,4,5-TCP, (f) 2,3,4,4-TECP. (h–j) High stability of the WN SERS substrate: (h) HRTEM image of the WN substrate after strong acid treatment. (i) HRTEM image of the WN substrate after strong base treatment. (j) HRTEM image of the WN substrate after 300 °C heat treatment. (j–l) Raman spectra of R6G obtained in various SCOM-TMN substrates: (j) MoN. (k) TiN. (l) VN.

Conclusion

In conclusion, the current work has developed a facile and general molten-salt/template strategy enabling the accurate preparation of TMN materials. Specifically, these TMN materials exhibit an uncommon SCOM structure, which provides a promising candidate with considerable research significance and application prospects for the TMN family. The combination of the molten salt method and template method is a valuable exploratory effort, which offers a methodological reference for the synthesis of high-lattice-energy TMNs with high specific surface area and porous characteristics. Hydroxylation and the subsequent formation of SCOM-structured metal oxides were identified as critical factors that govern the fabrication of TMNs with such SCOM structures. Additionally, due to the lack of intrinsic Raman scattering properties, these SCOM-WN substrates have effectively eliminated the background interference that plagues traditional non-metallic SERS substrates—this interference is primarily attributed to the inherent Raman signals of the latter. It is precisely the elimination of interference from their own Raman signals that has significantly enhanced the signal resolution of non-metallic SERS substrates, where the lowest detection limit and Raman EF are 1×10^{-12} M and 7.5×10^{7}, respectively. These SCOM-structured TMN materials are anticipated to substitute for noble metals in a wide range of applications within catalysis, energy storage, sensing technology, and other related fields.

Experimental section

Synthesis of MBA-15/OH

1.0 g of SBA-15 and 20 mL of hydrogen peroxide (30 wt%) in closed Teflon liner of 100 mL were heated at 100 °C for 5 h. After that, the sample was washed and freeze-dried at −80 °C to produce SBA-15/OH.

Synthesis of SCOM-WN

In a typical synthesis, 0.4 g of WCl_6 was taken and dissolved in 10 mL of anhydrous ethanol, and then 1 g of SBA-15/OH template was added under stirring at 200 r min^{-1} for 2 h with sufficient stirring. The solution was stayed overnight with the SBA-15 template, followed by separation of SBA-15/W-OH from ethanol using a centrifuge and vacuum freeze-drying at −80 °C. The dried product SBA-15/W-OH was fully mixed with KCl powder and heated to 600 °C at a rate of 1 °C min^{-1} under NH_3/N_2 conditions, kept for 1 h and then cooled down naturally. WN samples were obtained by washing the samples using deionized water and NaOH, respectively. In the synthesis of MoN, VN, TiN, and CoN, the tungsten source is simply replaced by a molybdenum source ($MoCl_3$), a vanadium source (VCl_3), a titanium source ($TiCl_3$), and cobalt chloride ($CoCl_2$).

Raman tests. To study the SERS properties of these as-synthesized SCOM-WN samples, a confocal micro Raman spectrometer (Renishaw-in Via Qontor) was used as the measuring instrument. In all SERS tests, unless specifically stated, the excitation wavelength is 532 nm, laser power is 0.5 mW, and the specification of the objective is ×50 L. A series of standard solution (aqueous) of R6G, with concentrations of 10^{-7}–10^{-12} M were used as the probe molecules. A series of standard solution of CV, MA, BPA, 2,4-DCP, 2,4,5-TCP, 2,3,5,6-TECP with concentrations of 1×10^{-7}–10^{-11} M were used as the probe molecules. To improve the signal reproducibility and uniformity, 20 mg of the SCOM-WN particles are immersed into the probe solution (30 mL) to be measured for 10 min, then taken out and dried in air for 10 min. In all SERS tests, the laser beam is perpendicular to the top of the sample to be tested with a resultant beam spot diameter of 5 μm. The fluorescent background of the probe molecule is deducted by the software that comes with the instrument.

Characterization. These samples were measured by a variety of characterization techniques. XRD patterns of the products were obtained on a Bruker D8 focus X-ray diffractometer by using CuKa radiation ($\lambda = 1.54178$ Å). XPS experiments are performed in an ESCALab 250Xi using monochromated Al Kα X-rays at $h\nu = 1486.6$ eV. Peak positions are internally referenced to the C 1s peak at 284.1 eV. SEM images were obtained on a HitachiS-4800. Ultraviolet-vis absorption spectra were recorded by a Shimadzu UV-3600-Plus with integrating sphere. TEM, HRTEM, and EDS characterizations were performed with a JEOL F200 operated at 200 kV. The specific surface area was measured in a Micro Tristar II 3020. Raman spectra were recorded from Renishaw-inVia Qontor.

Author contributions

G. C. X. conceived the project. Q. H. K. and J. L. supervised the research. L. C. Q. Y. and J. F. L. prepared materials and characterized and analyzed the data. Y. J. Z., W. C. Y. and M. Y. performed computational simulation. G. C. X. and L. C. Q. Y. wrote the paper. All authors engaged in discussions related to the manuscript.

Conflicts of interest

The authors declare no conflicts of interest.

Data availability

All data in the manuscript and supporting information (SI) can be obtained by contacting the corresponding author.

Supplementary information: the details of EF calculations, FDTD simulations, Fig. S1–S33, and Tables S1–S3. See DOI: https://doi.org/10.1039/d5sc09344a.

Acknowledgements

References

1 L. H. Bennett, J. R. Cuthill, A. J. McAlister, N. E. Erickson and R. E. Watson, Electronic Structure and Catalytic Behavior of Tungsten Carbide, Science, 1974, 184, 563–565.

2 J. E. Houston, G. E. Laramore and R. L. Park, Surface Electronic Properties of Tungsten, Tungsten Carbide, and Platinum, Science, 1974, 185, 258–260.

3 R. Zeng, Y. Yang, X. Feng, H. Li, L. M. Gibbs, F. J. DiSalvo and H. D. Abruña, Nonprecious Transition Metal Nitrides as Efficient Oxygen Reduction Electrocatalysts for Alkaline Fuel Cells, Sci. Adv., 2022, 8, eabj1584.

4 H. Hu, X. Wang, Z. Zhang, J. Liu, X. Yan, X. Wang, J. Wang, J. P. Attfield and M. Yang, Engineered Nickel–Iron Nitride Electrocatalyst for Industrial–Scale Seawater Hydrogen Production, Adv. Mater., 2025, 37, 2415421.

5 X. Song, Y. Li, M. Yin, J. Li, H. Yang, W. Liu, X. Wang and G. Xi, Multilayered Hollow Transition Metal Nitride Spheres Made from Single-Source Precursors for SERS Analytics, Nat. Commun., 2025, 16, 2678.

6 S. W. Robbins, H. Sai, F. J. DiSalvo, S. M. Gruner and U. Wiesner, Monolithic Gyroidal Mesoporous Mixed Titanium–Niobium Nitrides, ACS Nano, 2014, 8, 8217–8223.

7 L. Yang, L. Zhang, Y. Li, B. H. Lee, J. Kim, H. S. Lee, J. Bok, Y. Ma, W. Zhou, D. Yuan, A. L. Wang, M. S. Bootharaju, H. Zhang, T. Hyeon and J. Chen, Cation Exchange in Colloidal Transition Metal Nitride Nanocrystals, J. Am. Chem. Soc., 2024, 146, 12556–12564.

8 J. Guo, H. Zhao, Z. Yang, Y. Wang, X. Liu, L. Wang, Z. Zhao, A. Wang, L. Ding, H. Liu and X. Yu, Hierarchical Porous 3D Ni₃N–CoN/NC Heterojunction Nanosheets with Nitrogen Vacancies for High–Performance Flexible Supercapacitor, Nano Energy, 2023, 116, 108763.

9 H. Y. Jin, Q. F. Gu, B. Chen, C. Tang, Y. Zheng, H. Zhang, M. Jaroniec and S. Z. Qiao, Molten Salt–Directed Catalytic Synthesis of 2D Layered Transition–Metal Nitrides for Efficient Hydrogen Evolution, Chem, 2020, 6, 2382–2394.

10 R. Zeng, H. Li, Z. Shi, L. Xu, J. Meng, W. Xu, H. Wang, Q. Li, C. J. Pollock, T. Lian, M. Mavrikakis, D. A. Muller and H. D. Abruña, Origins of Enhanced Oxygen Reduction Activity of Transition Metal Nitrides, Nat. Mater., 2024, 23, 1695–1703.

11 X. Zhang, Y. Zhao, X. Jia, Y. Zhao, L. Shang, Q. Wang, G. I. N. Waterhouse, L. Z. Wu, C. H. Tung and T. Zhang, Silica–Protected Ultrathin Ni₃FeN Nanocatalyst for the Efficient Hydrolytic Dehydrogenation of NH₃BH₃, Adv. Energy Mater., 2018, 8, 1702780.

12 K. Li, B. Zhao, H. Zhang, H. Lv, J. Bai, H. Ma, P. Wang, W. Li, J. Si, X. Zhu and Y. Sun, 3D Porous Honeycomb–Like CoN–Ni₃N/N–C Nanosheets Integrated Electrode for High–Energy–Density Flexible Supercapacitor, Adv. Funct. Mater., 2021, 31, 2103073.

13 X. L. Zhang, P. C. Yu, S. P. Sun, L. Shi, P. P. Yang, Z. Z. Wu, L. P. Chi, Y. R. Zheng and M. R. Gao, In Situ Ammonium Formation Mediates Efficient Hydrogen Production from Natural Seawater Splitting, Nat. Commun., 2024, 15, 9462.

14 L. Lin, J. Liu, X. Liu, Z. Gao, N. Rui, S. Yao, F. Zhang, M. Wang, C. Liu, L. Han, F. Yang, S. Zhang, X. Wen, S. D. Senanayake, Y. Wu, X. Li, J. A. Rodriguez and D. Ma, Reversing Sintering Effect of Ni Particles on γ–Mo₂N via Strong Metal Support Interaction, Nat. Commun., 2021, 12, 6978.

15 L. Yang, H. Liu, Y. Li, L. Zhong, Z. Jin, X. Xu, D. Cao and Z. Chen, Customizing Bonding Affinity with Multi–Intermediates via Interfacial Electron Capture to Boost Hydrogen Evolution in Alkaline Water Electrolysis, Angew. Chem., Int. Ed., 2025, 64, e202414518.

16 Y. Li, H. Shao, Z. Lin, J. Lu, L. Liu, B. Duployer, P. O. Å. Persson, P. Eklund, L. Hultman, M. Li, K. Chen, X. H. Zha, S. Du, P. Rozier, Z. Chai, E. Raymundo-Piñero, P. -L. Taberna, P. Simon and Q. Huang, A General Lewis Acidic Etching Route for Preparing MXenes with Enhanced Electrochemical Performance in Non–Aqueous Electrolyte, Nat. Mater., 2020, 19, 894–899.

17 Y. Yuan, J. Wang, S. Adimi, H. Shen, T. Thomas, R. Ma, J. P. Attfield and M. Yang, Zirconium Nitride Catalysts Surpass Platinum for Oxygen Reduction, Nat. Mater., 2020, 19, 282–286.

18 G. Lin, H. Li and K. Xie, Twisted Surfaces in Porous Single Crystals to Deliver Enhanced Catalytic Activity and Stability, Angew. Chem., Int. Ed., 2020, 59, 16440–16444.

19 L. Eberle and J. Ballmann, Synthesis of Collidine from Dinitrogen via a Tungsten Nitride, J. Am. Chem. Soc., 2024, 146, 7979–7984.

20 Z. Yang, L. Wang, X. Zhang, J. Zhang, N. Ren, L. Ding, A. Wang, J. Liu, H. Liu and X. Yu, Nitrogen Vacancy Modulation of Tungsten Nitride Peroxidase–Mimetic Activity for Bacterial Infection Therapy, ACS Nano, 2024, 18, 24469–24483.

21 S. W. Robbins, H. Sai, F. J. DiSalvo, S. M. Gruner and U. Wiesner, Monolithic Gyroidal Mesoporous Mixed Titanium–Niobium Nitrides, ACS Nano, 2014, 8, 8217–8223.

22 X. Xiao, H. Yu, H. Jin, M. Wu, Y. Fang, J. Sun, Z. Hu, T. Li, J. Wu, L. Huang, Y. Gogotsi and J. Zhou, Salt–Templated Synthesis of 2D Metallic MoN and Other Nitrides, ACS Nano, 2017, 11, 2180–2186.

23 S. Xi, G. Lin, L. Jin, H. Li and K. Xie, Metallic Porous Nitride Single Crystals at Two–Centimeter Scale Delivering Enhanced Pseudocapacitance, Nat. Commun., 2019, 10, 4727.

24 M. Hasegawa and T. Yagi, Systematic Study of Formation and Crystal Structure of 3D–Transition Metal Nitrides Synthesized in a Supercritical Nitrogen Fluid under 10 GPa and 1800 K Using Diamond Anvil Cell and YAG Laser Heating, J. Alloy. Compd., 2005, 403, 131–142.

25 B. Forslund and J. Zheng, Carbothermal Synthesis of Aluminium Nitride at Elevated Nitrogen Pressures, J. Mater. Sci., 1993, 28, 3125–3131.

26 A. Djire, P. Pande, A. Deb, J. B. Siegel, O. T. Ajenifujah, L. He, A. E. Sleightholme, P. G. Rasmussen and L. T. Thompson, Unveiling the Pseudocapacitive Charge Storage Mechanisms of Nanostructured Vanadium Nitrides Using in–Situ Analyses, Nano Energy, 2019, 60, 72–81.

27 P. Chen, K. Xu, Z. Fang, Y. Tong, J. Wu, X. Lu, X. Peng, H. Ding, C. Wu and Y. Xie, Metallic Co$_4$N Porous Nanowire Arrays Activated by Surface Oxidation as Electrocatalysts for the Oxygen Evolution Reaction, *Angew. Chem., Int. Ed.*, 2015, **54**, 14710–14714.

28 K. Xu, P. Chen, X. Li, Y. Tong, H. Ding, X. Wu, W. Chu, Z. Peng, C. Wu and Y. Xie, Metallic Nickel Nitride Nanosheets Realizing Enhanced Electrochemical Water Oxidation, *J. Am. Chem. Soc.*, 2015, **137**, 4119–4125.

29 S. Joshi, Q. Wang, A. Puntambekar and V. Chakrapani, Facile Synthesis of Large Area Two–Dimensional Layers of Transition–Metal Nitride and Their Use as Insertion Electrodes, *ACS Energy Lett.*, 2017, **2**, 1257–1262.

30 C. Zhu, P. Yang, D. Chao, X. Wang, X. Zhang, S. Chen, B. K. Tay, H. Huang, H. Zhang, W. Mai and H. J. Fan, All Metal Nitrides Solid–State Asymmetric Supercapacitors, *Adv. Mater.*, 2015, **27**, 4566–4571.

31 H. Wang, E. J. Sandoz-Rosado, S. H. Tsang, J. Lin, M. Zhu, G. Mallick, Z. Liu and E. H. T. Teo, Elastic Properties of 2D Ultrathin Tungsten Nitride Crystals Grown by Chemical Vapor Deposition, *Adv. Funct. Mater.*, 2019, **29**, 1902663.

32 H. Guan, W. Li, J. Han, W. Yi, H. Bai, Q. Kong and G. Xi, General Molten–Salt Route to Three–Dimensional Porous Transition Metal Nitrides as Sensitive and Stable Raman Substrates, *Nat. Commun.*, 2021, **12**, 1376.

33 Z. Cui, P. Zhao, H. Wang, C. Li, W. Peng and J. Liu, Multi–Dimensional Ni@TiN/CNT Heterostructure with Tandem Catalysis for Efficient Electrochemical Nitrite Reduction to Ammonia, *Angew. Chem., Int. Ed.*, 2025, **64**, e202501578.

34 X. Xiao, H. Wang, W. Bao, P. Urbankowski, L. Yang, Y. Yang, K. Maleski, L. Cui, S. J. L. Billinge, G. Wang and Y. Gogotsi, Two–Dimensional Arrays of Transition Metal Nitride Nanocrystals, *Adv. Mater.*, 2019, **31**, 1902393.

35 Z. Mamiyev, N. O. Balayeva, D. R. T. Zahn and C. Tegenkamp, Enhanced Light–Matter Interactions With a Single Sn Nanoantenna on Epitaxial Graphene, *Adv. Optical Mater.*, 2025, **13**, e00979.

36 X. J. Tan, J. Melkersson, S. Q. Wu, L. Z. Wang and J. L. Zhang, *ChemPhysChem*, 2016, **17**, 2630–2639.

37 Q. D. Xia, Y. L. Jia, C. Bi, L. Y. Zhao, M. Yan, P. Shen, X. C. Zhang and S. K. Yang, Nanoporous Ag Microparticles with Tailorable and Noncontaminated Nanopores for SERS Sensing Applications, *Adv. Mater.*, 2025, **37**, 2414962.

38 D. C. Yang, B. Youden, N. Z. Yu, A. J. Carrier, R. Q. Jiang, M. R. Servos, K. D. Oakes and X. Zhang, Surface-Enhanced Raman Spectroscopy for the Detection of Reactive Oxygen Species, *ACS Nano*, 2025, **19**, 2013–2028.

39 Y. Yu, Y. J. Zong, T. Li, X. Z. Guo, W. C. Yi, M. Yin, J. F. Li, J. H. Zhang, Q. H. Kong and G. C. Xi, Single-Crystalline-Mesoporous TiN Nanosheets Free of Intrinsic Raman Scattering for Highly Sensitive Surface-Enhanced Raman Spectroscopy, *Anal. Chem.*, 2026, **98**, 934–943.

40 X. Song, Y. H. Li, M. Yin, J. F. Li, H. F. Yang, W. Liu, X. T. Wang and G. C. Xi, Multilayered hollow transition metal nitride spheres made from single-source precursors for SERS analytics, *Nat. Commun.*, 2025, **16**, 2678.

41 S. Lu, j. L. Li, W. P. Shen, Z. C. Wang, Y. C. Ma, X. Y. Su, Y. H. Lu, L. J. Li and Z. P. Chen, Two-Dimensional Atomically Thin Titanium Nitride via Topochemical Conversion, *ACS Nano*, 2023, **17**, 24299–24307.

42 X. L. Zhang, P. C. Yu, S. P. Sun, L. Shi, P. P. Yang, Z. Z. Wu, L. P. Chi, Y. R. Zheng and M. R. Gao, In situ ammonium formation mediates efficient hydrogen production from natural seawater splitting, *Nat. Commun.*, 2024, **15**, 9462.

43 L. Yang, H. B. Liu, Y. Li, L. S. Zhong, Z. H. Jin, X. P. Xu, D. P. Cao and Z. W. Chen, Customizing Bonding Affinity with Multi-Intermediates via Interfacial Electron Capture to Boost Hydrogen Evolution in Alkaline Water Electrolysis, *Angew. Chem., Int. Ed.*, 2025, **64**, e202414518.

44 J. Cao, T. Li, H. Gao, Y. Lin, X. Wang, H. Wang, T. Palacios and X. Ling, Realization of 2D Crystalline Metal Nitrides via Selective Atomic Substitution, *Sci. Adv.*, 2020, **6**, eaax8784.

45 H. Gao, D. Zhou, L. Ping, Z. Wang, N. T. Hung, J. Cao, M. Geiwitz, G. Natale, Y. C. Lin, K. S. Burch, R. Saito, M. Terrones and X. Ling, Downscaling of Non–Van Der Waals Semimetallic W$_5$N$_6$ with Resistivity Preservation, *ACS Nano*, 2025, **19**, 3362–3371.

46 S. Lu, J. Li, W. Shen, Z. Wang, Y. Ma, X. Su, Y. Lu, L. Li and Z. Chen, Two–Dimensional Atomically Thin Titanium Nitride via Topochemical Conversion, *ACS Nano*, 2023, **17**, 24299–24307.

47 Y. Qiu and L. Gao, Novel Synthesis of Nanocrystalline Gallium Nitride Powder from Gallium(III)–Urea Complex, *Chem. Lett.*, 2003, **32**, 774–775.

48 C. Giordano, C. Erpen, W. Yao and M. Antonietti, Synthesis of Mo and W Carbide and Nitride Nanoparticles via a Simple "Urea Glass" Route, *Nano Lett.*, 2008, **8**, 4659–4663.

49 X. T. Wang, W. X. Shi, S. X. Wang, H. W. Zhao, J. Lin, Z. Yang, M. Chen and L. Guo, Two-Dimensional Amorphous TiO$_2$ Nanosheets Enabling High-Efficiency Photoinduced Charge Transfer for Excellent SERS Activity, *J. Am. Chem. Soc.*, 2019, **141**, 5856–5862.

50 S. Cong, Y. Y. Yuan, Z. G. Chen, J. Y. Hou, M. Yang, Y. L. Su, Y. Y. Zhang, L. Li, Q. W. Li, F. X. Geng and Z. G. Zhao, Noble metal-comparable SERS enhancement from semiconducting metal oxides by making oxygen vacancies, *Nat. Commun.*, 2015, **6**, 7800.

51 Q. Q. Zhang, X. S. Li, Q. Ma, Q. Zhang, H. Bai, W. C. Yi, J. Y. Liu, J. Han and G. C. Xi, A Metallic Molybdenum Dioxide with High Stability for Surface Enhanced Raman Spectroscopy, *Nat. Commun.*, 2017, **8**, 14903.

52 J. Yu, C. Chen, Q. H. Zhang, J. Lin, X. Y. Yang, L. Gu, H. Zhang, Z. Liu, Y. Wang, S. Zhang, X. T. Wang and L. Guo, Au Atoms Anchored on Amorphous C$_3$N$_4$ for Single-Site Raman Enhancement, *J. Am. Chem. Soc.*, 2022, **144**, 21908–21915.

53 X. Tang, X. C. Fan, J. Zhou, S. Wang, M. Z. Li, X. Y. Hou, K. W. Jiang, Z. H. Ni, B. Zhao, Q. Hao and T. Qiu, Alloy Engineering Allows On-Demand Design of Ultrasensitive Monolayer Semiconductor SERS Substrates, *Nano Lett.*, 2023, **23**(15), 7037–7045.

54 H. Z. Sun, S. Cong, Z. H. Zheng, Z. Wang, Z. G. Chen and Z. G. Zhao, Metal–Organic Frameworks as Surface Enhanced Raman Scattering Substrates with High Tailorability, *J. Am. Chem. Soc.*, 2019, **141**, 870–878.

55 Y. Lin, P. Qi, J. Liu, Y. Zhuo, C. Cai, H. Zhang, X. Li, X. Liu, L. Chen, S. Luo and X. Tian, Large–Area Gold–Coated Polyamide Nanopillar Arrays Consisting of Secondary Lamellar Structures and Sub–10–nm Gaps for Ultrasensitive SERS Detection, *Adv. Mater. Technol.*, 2023, **8**, 2300367.

56 H. Y. Chen, M. H. Lin, C. Y. Wang, Y. M. Chang and S. Gwo, Large-Scale Hot Spot Engineering for Quantitative SERS at the Single-Molecule Scale, *J. Am. Chem. Soc.*, 2015, **137**, 13698–13705.